






## Unraveling the effect of collagen damage on bone fracture using in situ synchrotron microtomography with deep learning

Michael Sieverts <sup>1,5</sup>, Yoshihiro Obata <sup>1,5</sup>, James L. Rosenberg<sup>1</sup>, William Woolley<sup>1</sup>, Dilworth Y. Parkinson <sup>2</sup>, Harold S. Barnard<sup>2</sup>, Daniël M. Pelt <sup>3</sup> & Claire Acevedo <sup>1,4</sup>✉

When studying bone fragility diseases, it is difficult to identify which factors reduce bone's resistance to fracture because these diseases alter bone at many length scales. Here, we investigate the contribution of nanoscale collagen behavior on macroscale toughness and microscale toughening mechanisms using a bovine heat-treatment fragility model. This model is assessed by developing an in situ toughness testing technique for synchrotron radiation micro-computed tomography to study the evolution of microscale crack growth in 3D. Low-dose imaging is employed with deep learning to denoise images while maintaining bone's innate mechanical properties. We show that collagen damage significantly reduces macroscale toughness and post-yield properties. We also find that bone samples with a compromised collagen network have reduced amounts of crack deflection, the main microscale mechanism of fracture resistance. This research demonstrates that collagen damage at the nanoscale adversely affects bone's toughening mechanisms at the microscale and reduces the overall toughness of bone.

<sup>1</sup>Department of Mechanical Engineering, University of Utah, 1495 E 100 S, Salt Lake City, UT 84112, USA. <sup>2</sup>Advanced Light Source, Lawrence Berkeley Laboratory, 6 Cyclotron Rd, Berkeley, CA 94720, USA. <sup>3</sup>Leiden Institute of Advanced Computer Science, Leiden University, Niels Bohrweg 1, 2333 CA Leiden, The Netherlands. <sup>4</sup>Department of Biomedical Engineering, University of Utah, 36 S Wasatch Dr, Salt Lake City, UT 84112, USA. <sup>5</sup>These authors contributed equally: Michael Sieverts, Yoshihiro Obata. ✉email: [claire.acevedo@utah.edu](mailto:claire.acevedo@utah.edu)

Bone derives its unique resistance to fracture, also known as toughness, from its hierarchical structure spanning multiple length scales. This hierarchical structure includes bone's basic building blocks, primarily comprising collagen and mineral phases at the nanoscale, and osteonal structures (cylindrical features of concentric lamellae layers around a central Haversian canal) at the microscale<sup>1</sup> (Fig. 1a). Features at every length scale in the complex, composite structure of bone contribute to its characteristic high toughness and light weight<sup>2,3</sup>.

Of the many factors influencing toughness in bone, only changes in mineral content of the bone matrix are traditionally used to assess and predict fracture risk. While new, encouraging methods and aids for fracture risk assessment are being used in clinics such as trabecular bone score, bone material strength index, and computer-based algorithms (e.g., FRAX), the primary current clinical indicator of fracture risk is bone mineral density<sup>4–6</sup>. However, there is evidence that the mineral components mostly confer bone's elastic properties and strength<sup>7,8</sup> whereas collagen components predominantly contribute to bone's post-yield properties and failure energy<sup>9–11</sup>. Degraded and denatured collagen is prevalent in various conditions<sup>12,13</sup>, including age<sup>11,14</sup>, cancer<sup>15</sup>, osteogenesis imperfecta<sup>16–20</sup>, osteoarthritis<sup>21</sup>, osteoporosis<sup>22–24</sup>, diabetes<sup>25,26</sup>, and mechanical damage<sup>27</sup>. In these conditions, degraded collagen molecules usually result in a local unfolding or unwinding of the collagen

triple helix. This unfolding might be caused by the breaking of a small number of consecutive hydrogen bonds<sup>28–30</sup>. Collagen damage increases the risk of fracture in these populations and reduces bone's resistance to crack formation and crack growth<sup>14</sup>. Therefore, the role of factors beyond bone mineral density, such as collagen damage, should be considered when studying fracture in bone.

Fracture resistance in bone originates from both intrinsic and extrinsic toughening mechanisms<sup>31,32</sup>. Intrinsic (material) mechanisms act at the nanoscale and are known to impede crack initiation and growth in the plastic zone located around the crack tip<sup>31</sup> (Fig. 1c). This material plasticity around the crack tip is conferred by the collagen. Collagen's influence on bone's mechanical properties is influenced by many factors such as both enzymatic and non-enzymatic cross-linking<sup>33–35</sup> and molecular level bonds that depend on calcium ion content<sup>36</sup>. In contrast, extrinsic mechanisms act at length scales of tens to hundreds of micrometers in the wake of the crack<sup>37</sup> (Fig. 1b). Extrinsic toughening mechanisms use microstructural features to dissipate energy via crack deflection<sup>38</sup>, crack bridging, and microdamage accumulation<sup>39</sup>. The most dominant extrinsic toughening mechanism is crack deflection in the transverse direction<sup>37,40</sup>. Crack deflection is controlled by the direction of applied stresses driving crack growth and the anisotropy in bone's microstructure (e.g., highly mineralized cement line at the border of osteons in

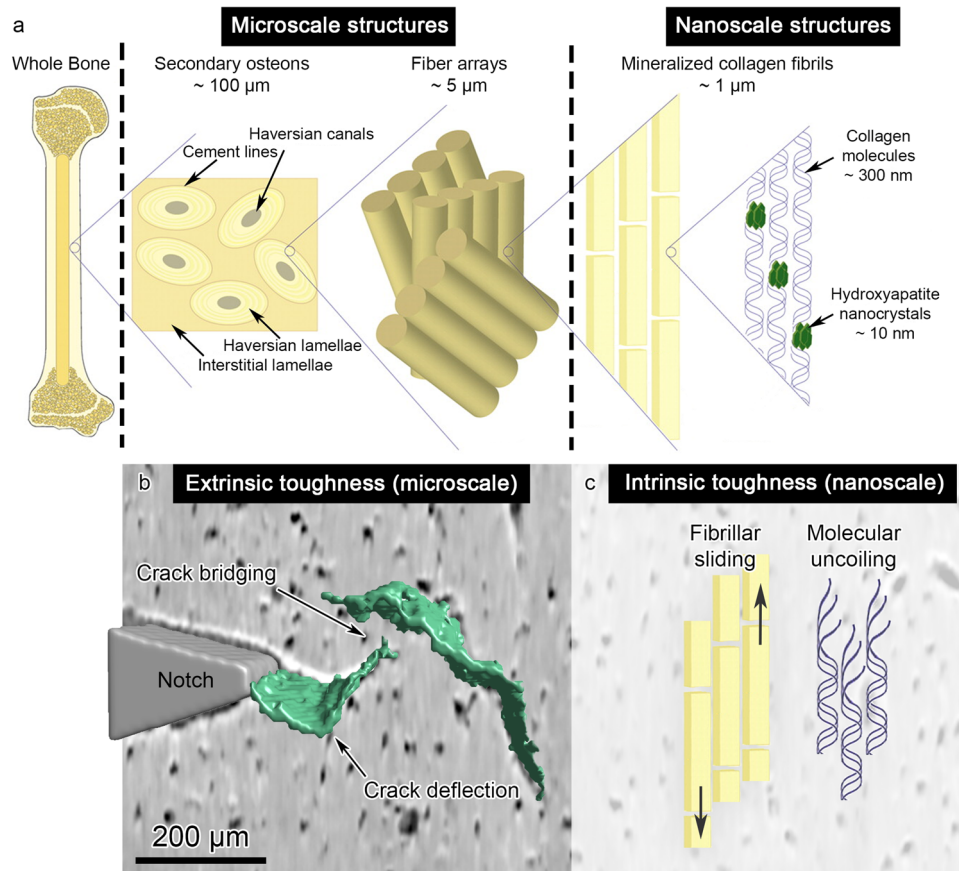


**Fig. 1 Overview of bone's hierarchical structure and bone's toughening mechanisms.** **a** Bone's hierarchical structure shows features ranging from the macroscale to the nanoscale. **b** Bone's extrinsic toughening mechanisms are illustrated using a 3D SRμCT image acquired during a toughness test. Extrinsic toughening mechanisms occur in the wake of the crack (green) and are attributed to microscale features in the bone. **c** Bone's intrinsic toughening mechanisms, which are attributed to nanoscale features, occur ahead of the crack and are primarily attributed to aspects of collagen structure and composition. Fibrillar sliding and uncoiling of the collagen structure are mechanisms that contribute to intrinsic toughness in bone. There are additional mechanisms that impact bone's intrinsic toughness, such as collagen cross-linking and sacrificial bonds. Collagen cross-linking at the nanoscale is known to influence mechanical properties<sup>34</sup>. Sacrificial bonds form between collagen fibrils creating a glue-like layer that contributes to bone's resistance to fracture<sup>32,36</sup>. Figure adapted from Zimmermann et al.<sup>115</sup>, with permission from The Proc. Natl. Acad. Sci. USA.

bone)<sup>41–43</sup>. In summary, intrinsic toughness absorbs energy via material properties and plastic deformation of collagen while extrinsic toughness dissipates energy primarily via crack deflection around microstructural features.

Extrinsic toughening has been shown to dissipate more energy than intrinsic toughening<sup>40</sup>. Therefore, changes in bone structure, such as canal diameter and density, would be the predominant contributor to toughness. However, this raises the questions of (1) whether bone's toughening mechanisms act independently or cooperatively; and (2) whether changes in material properties at the nanoscale, such as collagen damage, affect extrinsic toughening mechanisms at the microscale? Little is known about the contribution of collagen damage, present in many bone fragility diseases, to extrinsic toughness.

One advantageous modality for examining extrinsic toughening mechanisms in bone at the microscale is synchrotron radiation micro-computed tomography (SR $\mu$ CT). This technique uses high-flux x-rays to reconstruct an image stack corresponding to a scanned sample's three-dimensional (3D) structure and material composition<sup>44,45</sup>. Previous studies have shown that SR $\mu$ CT is able to reveal the crack path of a fractured bone sample<sup>41,46,47</sup>. With short acquisition times and high-resolution imaging, dynamic SR $\mu$ CT is well suited for in situ mechanical testing to determine how microstructure resists crack growth under realistic loading and failure conditions.

Deformation in bone during loading and failure conditions can be characterized in near real-time using digital volume correlation (DVC) with SR $\mu$ CT<sup>20,48,49</sup>. Presently, DVC has been more widely explored in trabecular bone, or porous bone, due to the unique, varied structure of the trabeculae<sup>50–53</sup>. In cortical bone, DVC can instead be performed by tracking the speckle-like osteocyte lacunae between different SR $\mu$ CT scans to estimate strain fields. Combining in situ mechanical testing in cortical bone with SR $\mu$ CT and DVC to obtain datasets of crack propagation with near real-time strain states would further elucidate crack growth mechanisms at the microscale.

However, in situ SR $\mu$ CT mechanical testing poses a fundamental challenge: overirradiation of bone during high-resolution SR $\mu$ CT imaging. Radiation impairs bone's mechanical properties when exposures reach a cumulative dosage of 35 kGy and above<sup>54–56</sup>. Acquiring lower-quality scans using a reduced radiation dose can aid in maintaining mechanical properties<sup>53</sup>. The preservation of mechanical properties with low-dose scans comes at the cost of a reduced signal-to-noise ratio<sup>56</sup>. In turn, features in these low-dose images cannot successfully be segmented, eliminating the possibility of performing DVC. Our solution to this issue is leveraging deep learning to process low-quality images prior to DVC.

In recent years, deep learning has shown promise in noise removal and enhancing the signal of images<sup>57–59</sup>. Specifically, convolutional neural networks (CNNs) have had success in denoising and segmenting images in the biomedical engineering field<sup>60</sup>. Performing these tasks with CNNs provides an unprecedented opportunity to enable SR $\mu$ CT imaging with lower radiation and accelerate image analysis. To our knowledge, the use of CNNs in conjunction with low-dose SR $\mu$ CT imaging to enable damage-mitigated DVC has not previously been performed.

This work aims to determine the role of collagen deformation capacity on the fracture resistance of bovine cortical bone. Our hypothesis is that alteration of the collagen network, often associated with aging and fragility diseases, results in decreased crack deflection and reduced bone toughness. To test this hypothesis, we used a heat-treatment model since the rate of local unfolding of collagen and cleavage at the unfolded sites rapidly is known to increase with temperature<sup>16</sup> in a similar way to unfolding progression with pathological conditions<sup>14</sup>. We examined changes in

whole-bone fracture resistance, microscale deformation, and crack path for different levels of collagen denaturation. To achieve this aim, we have developed the promising technique of in situ SR $\mu$ CT testing, which combines low-dose synchrotron imaging of cortical bone with CNNs for near real-time insight into crack evolution during mechanical testing. We discovered that damaging the collagen through heat treatment decreased macroscale toughness and post-yield mechanical properties in the transverse direction of bovine bone. Decreases in macroscale toughness due to collagen damage were evident in reduced amounts of crack deflection. These deflections tended to be informed by the internal strain state estimated using DVC. This work concludes that collagen damage, induced via heat treatment, at the nanoscale profoundly affects both microscale crack deflection and macroscale mechanical properties.

## Results

### Collagen damage and fragility induced through heat treatment.

A set of bovine bone samples ( $N = 8–11$ /group) were dedicated for use in a biochemical assay to quantify collagen denaturation via local unfolding and the associated decrease in flexural strength. Since the rate of local unfolding increases with temperature<sup>16</sup>, heat denaturation is a good model to induce a similar local triple helix unfolding to pathologic conditions. Samples were heat-treated for two hours at temperatures in the range known to denature mineralized collagen (100 °C to 190 °C). Heat treatment can either be reversible when the collagen molecule regains its original structure at normal temperature, or permanent with irreversible unfolding or damage of triple helical structure into an uncoiled structure<sup>28</sup>.

Samples heat treated above 130 °C sustained permanent collagen damage while samples treated at, or below, 130 °C were significantly less damaged. Denatured collagen chains, which are non-helical and unfolded, are susceptible to cleavage by proteases, including trypsins<sup>61–63</sup>, whereas intact triple helix collagen chains are not<sup>15</sup>. Therefore, we used a trypsin assay to digest and quantify the amount of damaged collagen (DC) combined with hydroxyproline assay to quantify the amount of undamaged collagen (UC) to calculate the percentage of DC in each bone sample<sup>64</sup>. Minimal collagen damage ( $\leq 3\%$ ) was present in samples at or below 130 °C, whereas considerably more damage was detected in samples treated at 160 °C or above (Fig. 2a). These results confirm that collagen damage onset occurs between 130 °C and 160 °C. As such, bones treated at 130 °C and below were considered in this study as UC groups and bones treated at 160 °C and above can be considered as DC groups.

We assessed the effect of heat treatment on bovine bone's mechanical properties with a flexural strength test using a set of bovine bone samples ( $N = 6–8$ /group) dedicated for mechanical testing divided into the same heat-treatment groups (Fig. 2c–e). For ultimate strain and work to fracture, the 160 °C and 190 °C groups were significantly lower compared to all other groups. We observed a significant reduction in ultimate strain and work to fracture in the DC groups ( $p < 0.001$ ); however, no change was observed in Young's Modulus ( $p = 0.889$ ) between the UC and DC groups (Fig. 2c–e). The exact values, standard deviations, and statistical significance for each group are shown in Supplementary Table 1. These findings indicate that collagen damage mostly affects post-yield properties. Results from the flexural test further confirm that significant collagen damage occurs in temperatures between 130 °C and 160 °C.

**High-quality SR $\mu$ CT imaging achieved with a low-radiation dose using deep learning.** The repeated imaging involved with fracture analysis necessitated acquiring images at lower doses of

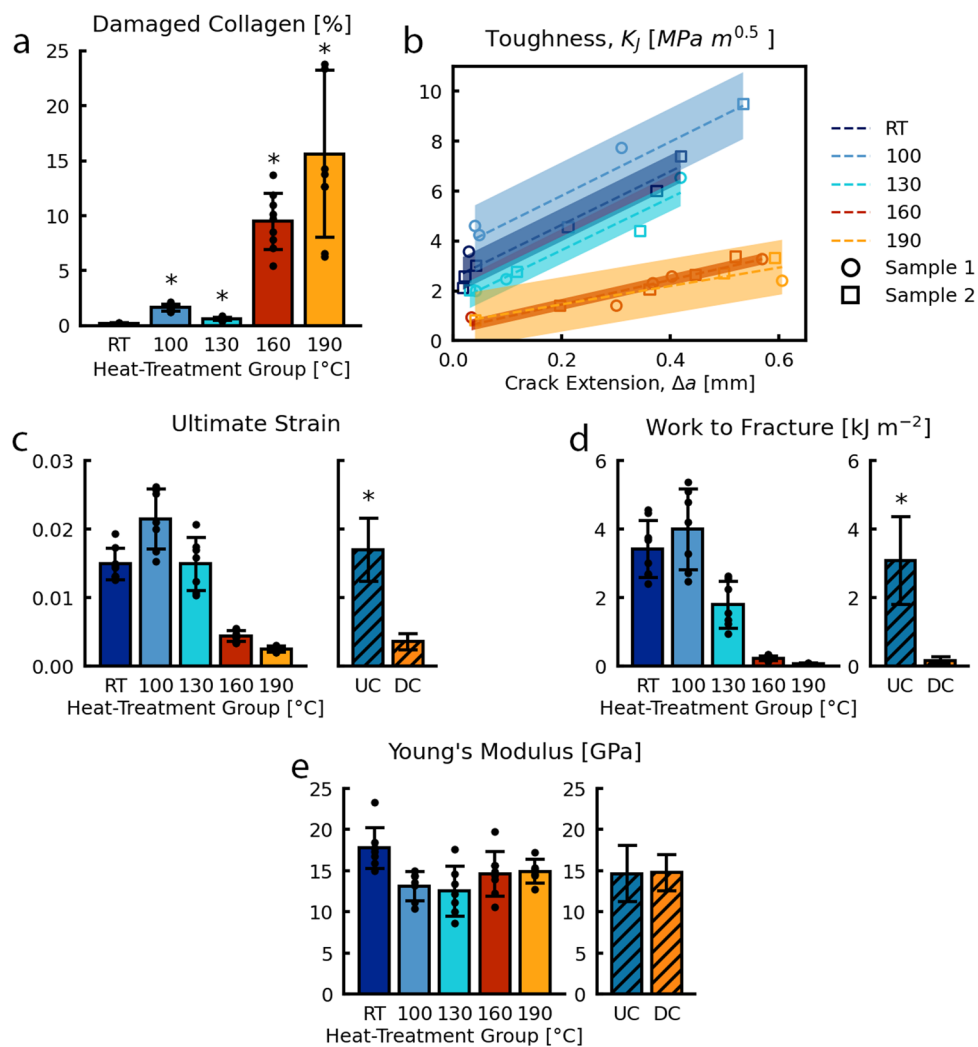


**Fig. 2 Collagen damage is evident in results from biochemical, fracture toughness, and mechanical tests.** Based on the trypsin-hydroxyproline assay, two general categories of collagen damage were defined. The two groups were undamaged collagen (UC), including samples from RT, 100 °C, and 130 °C, and damaged collagen (DC), including the 160 °C and 190 °C samples. All bar-chart data are represented by mean  $\pm$  standard deviation. **a** The trypsin-hydroxyproline assay ( $N = 8-11/\text{group}$ ), which measures the percent of damaged collagen, shows an increase in collagen damage with increases in heat-treatment temperature. Very little collagen damage was present in RT, 100 °C, and 130 °C groups. The 160 °C and 190 °C groups possessed much more damage than the lower-temperature groups. A Tukey multiple comparison tests showed that all groups were significantly different from one another. **b** The crack-resistance curves (R-curves) from the in situ SR $\mu$ CT toughness test ( $N = 2/\text{group}$ ) shows a marked decrease in toughness from the UC groups to the DC groups. **c** Flexural strength tests ( $N = 6-8/\text{group}$ ) were performed to obtain ultimate strain, work to fracture, and Young's modulus. The ultimate strain was reduced from the UC groups to the DC groups. A Tukey test revealed that all temperatures were significantly different from each other except the RT and the 130 °C. **d** Work-to-fracture was greatly reduced from the UC groups to the DC groups. Tukey test showed that all groups were significantly different from each other except the RT and 100 °C, and the 130 °C and 160 °C. **e** Young's modulus is largely unaffected by heat treatment; there was no significant difference between the UC and DC groups. A Tukey test revealed that the groups that were significantly different from each other include the RT and 100 °C, and the RT and 130 °C.

radiation to preserve bone's mechanical integrity. Low-dose radiation imaging produced noisy images that would not be feasible to use in further analysis. The quality of these images was improved with deep learning using a mixed-scale dense CNN<sup>65</sup>. The CNN accepted low-quality images as input and used high-quality images as the target (Fig. 3a, b). The trained CNN was able to greatly reduce the difference between the low- and high-quality images, resulting in improved image quality (Fig. 3g).

Images denoised with the CNN increased in similarity to the high-quality images. Mean-squared error (MSE) was used to measure how different images were from the high-quality images, and peak signal-to-noise ratio (PSNR) was used to measure how similar images were to the high-quality images. The CNN denoising decreased the low-dose image's MSE by 85% (Fig. 3)

and increased the low-dose image's PSNR by 62% on the holdout test dataset (Supplementary Figure 1). Reviewing the images qualitatively, we observed that images processed with the CNN had increased contrast between the bone and the background compared to the low-quality and the high-quality images. The corresponding image grayscale intensity histograms further illustrate this observation. The histograms for the low- and high-quality images both have a single peak, while the histograms for images processed with the CNN have two distinct peaks, one small peak for the background and one larger peak for the bone (Fig. 3a-c). Having the voxels distributed into these two peaks allows for more precise and consistent image segmentation. The denoised CNN output appears to have a higher signal-to-noise ratio than the high-dose target images used during training. This

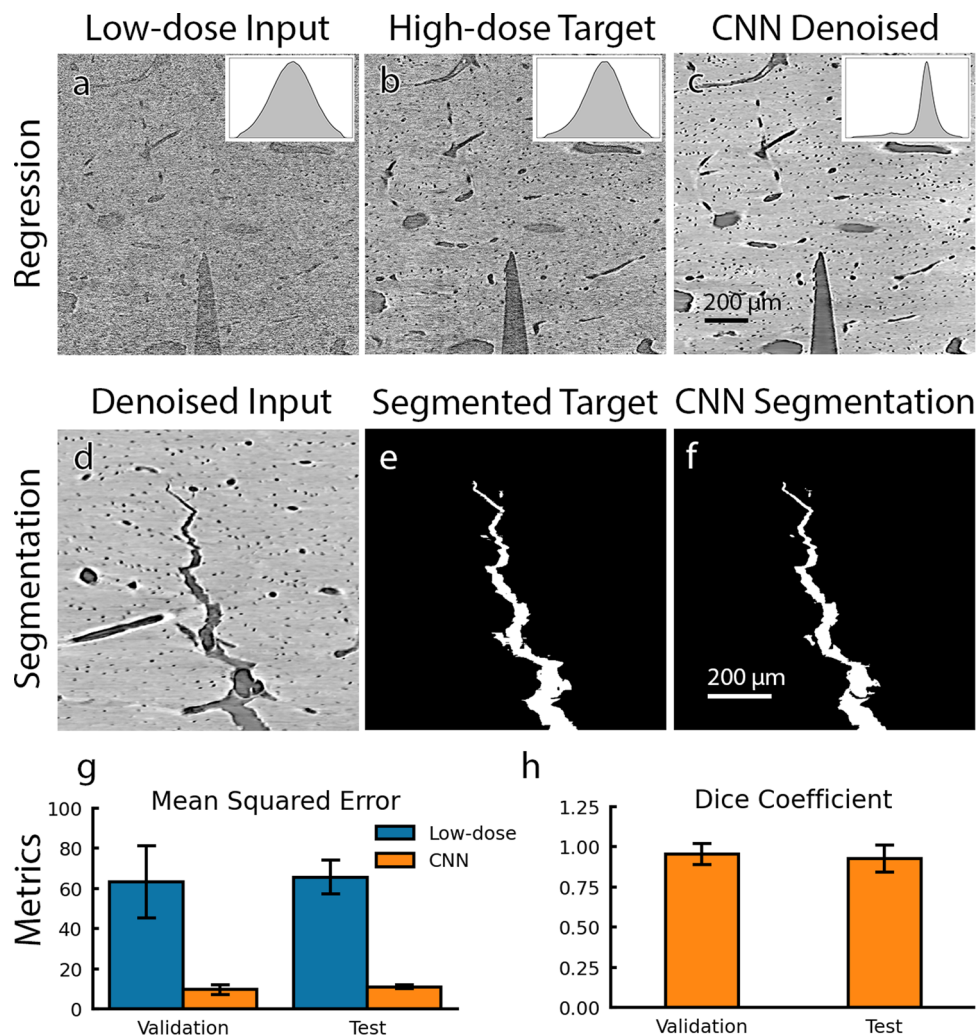


**Fig. 3** The CNN successfully denoised and segmented SR $\mu$ CT images acquired with low radiation. **a–c** Example of images related to the regression, or denoising, functionality of the CNN. Left to right these images include **a** the low-quality image used as input to the CNN, **b** the corresponding target image that is used during training, and **c** the denoised output from the CNN. Each image has its corresponding histogram included in the top right corner. **d–f** Example images related to the segmentation capabilities of the CNN. Left to right these images include **d** the denoised image used as input for segmentation, **e** the manual segmented image referenced during training, and **f** the segmentation performed by the CNN. **g** MSE was used to assess how well the CNN removed noise from the input image. In both the validation and the test datasets the CNN output was much more similar to the target than the input low-quality image. **h** Segmentation performance was evaluated with the Dice coefficient. This coefficient ranges from 0 to 1 where 1 is perfect segmentation. The network achieved high Dice coefficients for both the validation and the test datasets. All bar-chart data are represented by mean  $\pm$  standard deviation.

behavior could be caused by noise in the high-dose target images being uncorrelated to the noise in the low-dose input images, which is similar to the explanation for the denoising performance of self-supervised deep-learning methods<sup>58,66</sup>.

We made further use of CNN to expedite image analysis with semantic segmentation. Segmenting the crack path from the background and other features in the scan is a necessary process for analyzing the crack properties. This process was accelerated using CNN. The network accepted denoised images as input (Fig. 3d) and used a manual segmentation of the crack as a target image (Fig. 3e). The CNN's performance was evaluated by calculating the Dice similarity coefficient<sup>67</sup>. The Dice coefficient indicates how well the segmentation corresponds to the ground truth, where 0.0 is a completely incorrect segmentation and 1.0 is a perfect segmentation. The CNN performed the segmentation task well with the mean Dice coefficients for the network's segmentation being close to 1.0 (0.96 validation, 0.93 test) (Fig. 3h). Qualitative inspection of the segmentation also

indicated that the network was performing the task appropriately (Fig. 3d–f). An example of crack segmentation for each step in toughness testing is shown in Supplementary Movie 1 for a 160 °C sample.

**Fracture toughness is impaired by collagen damage.** Fracture toughness was evaluated using a set of bovine bone samples ( $N = 2/\text{group}$ ) dedicated to in situ SR $\mu$ CT toughness testing. Crack-resistance curves, or R-curves, are reported in terms of crack-driving stress-intensity factor,  $K$ , with respect to stable crack extension,  $\Delta a$ . R-curve data revealed that crack initiation toughness is markedly reduced in the DC groups compared to the UC groups, with DC groups having between two to three times lower crack initiation toughness than UC groups (1.39 MPa  $\cdot$  m<sup>1/2</sup> and 3.15 MPa  $\cdot$  m<sup>1/2</sup>, respectively, see Supplementary Table 1). Crack-growth toughness (slope of the R-curve) of bone samples from DC groups was reduced to one-third the value of UC groups

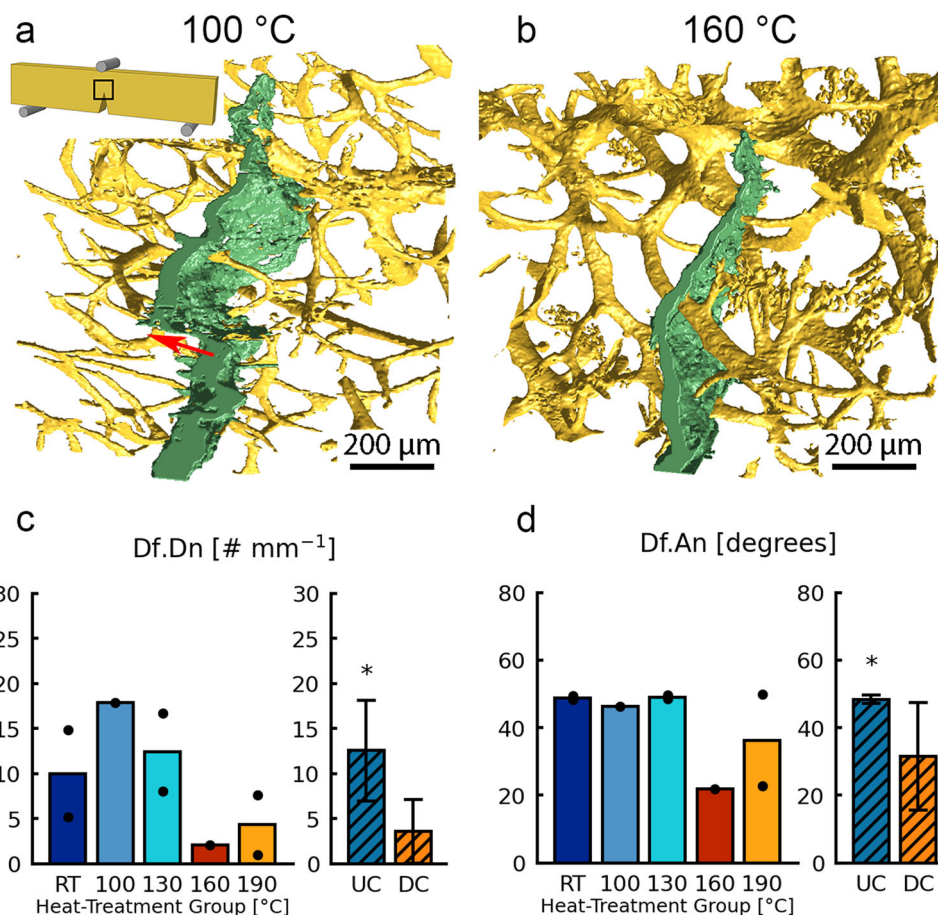


**Fig. 4** The amount of crack deflection was reduced due to damaged collagen. **a, b** Segmentation of bone samples after toughness testing, with canals colored in yellow and the crack path colored in green for both 100 °C and 160 °C samples. The red arrow indicates a large crack deflection in a 100 °C sample. **c** Crack deflection density, number of crack deflections per length of crack extension (Df.Dn), was reduced in the DC groups compared to the UC groups. **d** The average angle of crack deflection (Df.An) shows that UC groups exhibit more salient crack deflection than DC groups. In graphs, **c, d** the bars for each temperature represent the mean and each data point is shown as a black dot ( $N = 1-2/\text{group}$ ). The bars for the UC and DC groups show the mean and standard deviation ( $N = 3-5/\text{group}$ ).

(Fig. 2b). The toughness of UC groups at  $\Delta a = 0.4$  mm is almost triple its crack initiation toughness value ( $2.5-7 \text{ MPa} \cdot \text{m}^{1/2}$ ), whereas it is only double in DC groups ( $1-2 \text{ MPa} \cdot \text{m}^{1/2}$ ). The R-curve behavior and trypsin-hydroxyproline assay results exhibited here imply that heat treatment beyond 130 °C reduces macroscale fracture toughness in the transverse direction of bone through collagen damage.

**Crack deflection is impaired in collagen-damaged bone via heat treatment.** Through denoising and segmentation of low-radiation-dose images using the CNN, we examined microscale crack-growth mechanisms with the in situ SR $\mu$ CT image data. Crack deflection reduction was observed via SR $\mu$ CT images (Fig. 4a, b) in DC group with reduced R-curve toughness behavior. Crack morphology was also quantified with several parameters. Crack deflection density (Df.Dn), i.e., the number of large crack deflections per millimeter of crack extension, was significantly higher in the UC groups than in the DC groups (Fig. 4c). A concurrent significant increase in average deflection angle (Df.An) was also observed in UC groups compared to the DC groups (Fig. 4d). Through Df.Dn and Df.An, the extrinsic toughness mechanism of crack deflection is unmistakably impaired with heat treatment beyond 130 °C. The reduced presence of crack deflection in the DC groups is accompanied by a decrease in overall toughness, exemplified by the R-curve data

(Fig. 2b), reinforcing the importance of crack deflection as a salient toughening mechanism in bone.

**Internal strain state dictates the evolution of crack propagation.** Observing the importance of crack deflection led to using our in situ toughness testing technique to determine how internal strain influences crack deflection during a loading scenario. We performed DVC by tracking the displacement of osteocyte lacunae on SR $\mu$ CT images acquired at various steps during the three-point bend fracture toughness test, revealing bone's internal strain state for varying levels of heat treatment. Although all groups had two characteristic lobes of high-strain concentration near the tip of the notch, the strain extended laterally into the bone sample, further away from the crack, in the UC samples (Fig. 5b) compared to the DC samples (Fig. 5h).

Visualizing the internal strain of a bone sample during a fracture toughness test after crack initiation is beneficial alone, and overlaying this strained state into context with the next step in crack propagation provides additional insight into fracture mechanisms. We visualized the relationship between strain state and fracture path by overlaying the strain state calculated at crack initiation with the following step of crack propagation (Fig. 5c, f, i, l). We observed that the crack propagated through regions of high strain in each image slice, and when rendered in 3D. Because in the UC samples the internal strain was high in regions further

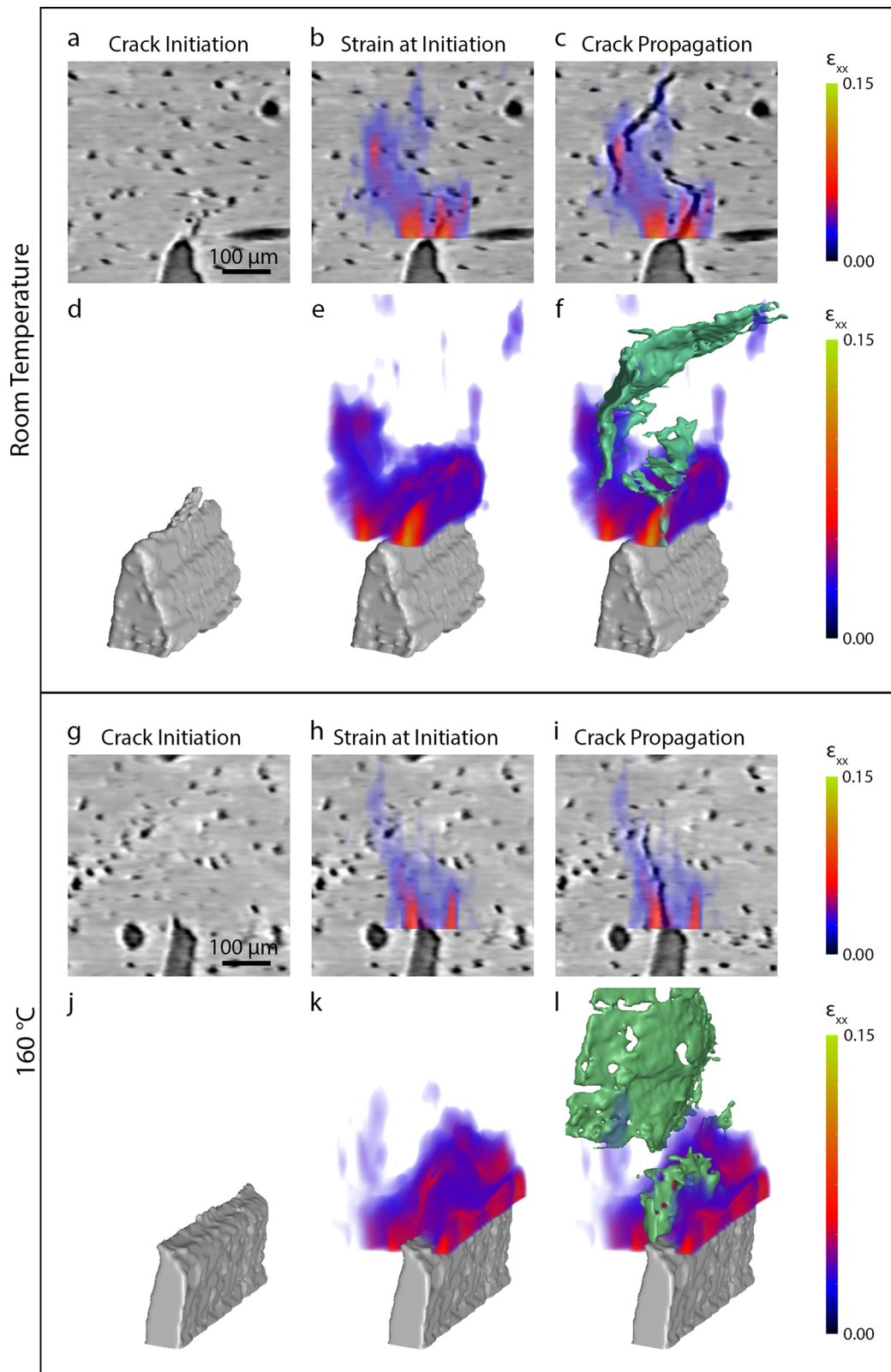


**Fig. 5 The internal strain state, revealed by DVC, informs the trajectory of crack propagation.** This is visualized by overlaying the strain ( $\epsilon_{xx}$ ) on images of the notch and crack. Left to right, all images show an image of crack initiation, the image of crack initiation with the corresponding strain state overlaid, and the strain state at crack initiation overlaid on the image of the next step of crack propagation. In the 3D images the notch is colored in gray and the crack is colored in green. **a-c** Examples of 2D DVC results for a room temperature sample. **d-f** Corresponding examples of 3D DVC results for a room temperature sample. **g-i** Examples of 2D DVC results for a 160 °C sample. **j-l** Corresponding examples of 3D DVC results for a 160 °C sample.

from the initial crack, more deflections towards these regions occurred, resulting in a tortuous crack path (Fig. 5c, f). In contrast, the crack path in the DC samples tended to propagate directly in the direction of mode I fracture, or fracture in the opening direction of the crack, following its corresponding prior strain state.

## Discussion

Bone fragility is a complex pathology caused by a variety of conditions. Traditionally, fractures were attributed to a reduction in bone mineral density; however, this metric describes less than half of bone fractures<sup>68,69</sup>. This discrepancy illustrates one of the reasons an increased emphasis has been placed on understanding bone quality in both research and clinical settings<sup>70,71</sup>. The goal of this study is to evaluate the unique contribution of collagen damage to bone quality, specifically on bone's properties that resist fracture. For this purpose, we used heat-treatment to model bone fragility in bovine cortical bone based on different levels of collagen molecular damage associated with molecular unfolding at different temperatures (Room Temperature, 100 °C, 130 °C, 160 °C, and 190 °C)<sup>72–74</sup>. This model was chosen to identify collagen damage's independent contribution to bone's resistance to fracture. To capture the evolution of microcracks in bone during mechanical loading, we developed an *in situ* SR $\mu$ CT toughness testing technique for bone and other biological tissues. This research is, to our knowledge, the first dynamic experimental analysis quantifying toughening mechanisms, specifically crack deflection, and deformation evolution within bone samples with different levels of fragility during mechanical testing. We leveraged a CNN for denoising and segmentation to work in tandem with low-radiation dose imaging to mitigate the destructive effects of overirradiation due to high-flux synchrotron x-rays. This technique revealed that unfolding and damage of collagen at the nanoscale affect the predominant toughness mechanisms at the microscale (i.e., crack deflection), reducing the macroscale toughness and bone quality. Understanding the contribution of collagen damage provides insight into the origins of bone fragility and collagen quality.

In this work, we found using a trypsin-hydroxyproline assay that a large increase in the amount of (mineralized) collagen damage in bone was observed in the 160 °C and 190 °C groups (Fig. 2). These findings are consistent with the literature, as denaturation of mineralized collagen in cortical bone has been shown at temperatures between 150 °C and 160 °C<sup>72,74,74–77</sup> whereas non-mineralized collagen in soft tissues denatures through unfolding around 60 °C. Wang and colleagues report the start of collagen damage occurring at temperatures of 120 °C also using trypsin-hydroxyproline assay; however, the largest increase in DC was found at 160 °C in their work<sup>78</sup>. Heat treatments below 200 °C do not alter the composition and the crystal structure of the mineral phase<sup>78–80</sup>. X-ray diffraction has shown that the inorganic phase of bone is not significantly altered at temperatures ranging from 100 °C to 200 °C<sup>72,81,82</sup>. Therefore, the heat treatment groups only induce collagen network damage without altering the mineral phase which confers bone's elastic properties. This was confirmed by the fact that Young's modulus did not change significantly between room temperature and 190 °C in the present work and in the work by Wang and colleagues<sup>78</sup>. Although the inorganic phase of bone is likely unaffected by heat treatment, heat treatment also dehydrates bone tissue. Dehydration is known to reduce bone's mechanical properties when not rehydrated<sup>83,84</sup>. Granke et al.<sup>84</sup> find that water eliminated at temperatures below 200 °C is the loosely- to tightly bound water in collagen. Additionally, rehydration of bovine bone in a saline solution that has been dehydrated in alcohol seems to restore its

mechanical properties<sup>85</sup>. Therefore, rehydration of bone samples at least 12 hours before testing preserves the majority of bone's mechanical properties.

Our results indicate that collagen damage within bone decreases bone's material properties at the macroscale. This decrease in mechanical properties was shown by significant reductions in fracture toughness, ultimate strain, and work to fracture in groups that had substantial collagen damage. For example, *in situ* SR $\mu$ CT toughness testing on notched samples with different levels of collagen damage showed a 50–70% decrease in crack initiation and crack growth in bone's with >3% DC. For bone in the UC groups (<3% DC), our R-curve toughness values are consistent with the ones found in the literature for toughness testing in bovine bone. Crack initiation toughness was observed at 3.2 MPa · m<sup>1/2</sup> in a study by Sakakura and Pezzotti, very similar to values in the RT group; however, the crack growth toughness (R-curve slope) in our study was notably higher than the slope in the Sakakura and Pezzotti study<sup>86</sup>. Similarly, work by Lucksanasombool et al. reports crack initiation toughness at 3.48 MPa · m<sup>1/2</sup><sup>85</sup>. Other studies report crack initiation toughness in the range of 2.4–5.2 MPa · m<sup>1/2</sup> in the transverse direction, falling in the range of values observed in the present study<sup>87,88</sup>. Crack initiation and crack growth toughness observed in our study are comparable to past studies using bovine bone in the transverse direction.

We observed that collagen damage induced by heat treatment not only reduced the bone's resistance to crack initiation but also the salience of crack deflection during crack growth. Reduction in bone's resistance to crack initiation due to collagen damage is an expected intrinsic toughening effect since heat treatment impairs bone's postyield, or plastic, properties. Osteonal microcracking also influences fracture in bone prior to crack initiation<sup>89</sup>; however, once the crack has been initiated, bone's resistance to crack growth is expected to be largely unaffected by changes to plastic properties because bone's predominant toughening mechanism during crack growth in the transverse direction is crack deflection<sup>32,37,39</sup>. In the transverse direction, cement lines around osteons act as surfaces of least resistance for crack growth, causing a propagating crack to suddenly change direction, dissipating energy during crack deflection. We observed that collagen damage induced by heat treatment resulted in a trend towards less frequent and less severe large crack deflections. Increased collagen damage was associated with three times fewer crack deflections and a 15° reduction in crack deflection angle. Past studies have attributed crack deflection solely to changes in micro- and macrostructure, such as increased osteonal density and orientation<sup>90</sup>. While these factors are integral to crack deflection and other extrinsic toughness mechanisms in bone, they don't address material properties below the microscale.

Fantner et al.<sup>82</sup> showed that heat-treatment-induced collagen damage drastically reduces bone's ability to maintain fibrillar connections between fracture surfaces, or collagen fibril bridging, in trabecular bone. This past work helps to corroborate that heat treatment-induced collagen damage reduces bone's capability to impair fracture at the microscale. The present work builds on previous work primarily by constructing an R-curve using *in situ* toughness tests, and by investigating the toughening mechanism of crack deflection, as opposed to collagen fibril bridging. The measures of Df.Dn and Df.An (Fig. 4) indicates a drop in the saliency of crack deflection with heat treatment above 130 °C. Fantner et al. also show a marked change crack growth behavior in heat-treated bone, but from the perspective of collagen fibril bridging; heat-treatment at 200 °C revealed no collagen fibril bridging compared to an untreated sample with many collagen fibrils spanning the crack. The reduced influence of collagen fibril bridging at 200 °C in trabecular bone found by Fantner et al. and



the reduced salience of crack deflection in cortical bone samples heated at 190 °C in this work show that different toughening mechanisms are impaired in collagen-damaged trabecular and cortical bones. Willet et al.<sup>91</sup> also observed that collagen plays a role in both intrinsic and extrinsic toughening mechanisms. Isolating collagen damage identified a unique effect of collagen intrinsic mechanisms on extrinsic toughening mechanisms. This effect indicates that intrinsic and extrinsic toughness may act cooperatively and that changes in collagen plasticity affect both intrinsic and extrinsic toughening mechanisms significantly.

By visualizing the strain distribution using DVC, we observed that the prior strain state informed the trajectory of crack propagation during the next step of loading. In the heat-treated samples, the strain state appeared more confined to the region around the crack tip compared to the groups without much collagen damage. This difference could be related to the reduction in crack deflection observed in the groups with collagen damage. The reduced crack deflection, or a smooth fracture profile, in the DC groups, is one of the indicators used by Zioupos et al to categorize bone samples as brittle<sup>92</sup>. Recently, the application of DVC to reveal strains in trabecular bone has received much attention<sup>51–53</sup>. Conversely, little work has been published on applications of DVC in cortical bone<sup>93–95</sup>. In this work, we further develop the application DVC in bone by imaging at a resolution that allows for analysis of tissue level strains within cortical bone while still addressing the issue of overirradiation.

Our study has several limitations starting with low sample size. Because access to a synchrotron beamline is provided based on merit in 24–72 hour shifts, performing an experiment with five groups and acceptable sample size for statistical analysis is challenging; our sample size was achieved in a 48-hour beamtime shift. Future studies using fewer groups could achieve higher statistical power with this in situ toughness testing technique. To achieve a reasonable sample size for comparison, groups in this study were combined into UC and DC groups based on the trypsin-hydroxyproline assay results. Additionally, while heat treatment was deemed a simple and effective method of targeting the collagen structure to pilot the in situ toughness testing technique used here, the manner in which heat treatment denatures collagen is not a direct analog for the complex pathways that disease disrupts collagen. The heat treatment (at temperatures at and above 160 °C) not only unfold the collagen molecules but might also affect the bonding and cross-linking in the collagen environment and weaken the mineral-collagen interface<sup>72,78</sup>. By showing the capability of this in situ SRμCT testings here, future work can be focused on using this technique on bone tissue damaged by disease. It is also worth noting that cortical bone from adult bovine is a mix of Haversian and plexiform whereas cortical bone from adult humans is mostly Haversian<sup>96–98</sup>. We worked with the posterior femoral mid-diaphysis which has a Haversian-dominated microstructure with well-formed osteons. However, there is the possibility that regions of plexiform combined with Haversian bone could be present, as these intermixed regions have been observed in the work of others<sup>96,97</sup>. Finally, although DVC provided useful visualizations of the strain distribution within bone, it is possible that some of the strain values are exaggerated due to microcracks occurring below our image voxel size of 1.6 μm<sup>89</sup>. The accuracy of the strains calculated with DVC also remains to be validated. Despite these limitations, DVC provides unique insight into displacements and strains resulting from cortical bone mechanics, and shows promise in informing crack deflection and brittle fracture in bone.

The work performed here in cortical bone demonstrates how damage to collagen at the nanoscale adversely affects crack deflection at the microscale and reduces overall toughness in the transverse direction at the macroscale. These findings were only

achieved through the development of an in situ SRμCT mechanical testing technique that combines low-dose imaging with deep learning denoising and segmentation. The valuable insight provided by this new technique can be applied to study pathologies known to impact bone toughness. This technique is especially useful in studying pathologies that impact bone quality while not affecting bone mass, such as diabetes. Our findings relating collagen damage via heat treatment directly to crack deflection show how bone's most fundamental constituent at the nanoscale affects toughness at each subsequent length scale in the hierarchical structure of bone.

## Methods

**Sample preparation.** All samples used in this study were machined from the mid-diaphysis of 18-month-old female bovine femurs. Whole bone was cut into four quadrant sections of ~40 mm long, under constant DI water irrigation. The posterior quadrant, presenting the most osteons, was kept for further cutting process. Cortical bone samples were cut with a low-speed diamond saw along the longitudinal axis of the femur. The posterior quadrant was fixed following the bone's long axis, then bone samples were cut with precise parallel cuts. Samples were ground and polished under constant DI water irrigation into dimensions of 1 mm × 2 mm × 10 mm. Samples used in toughness testing were notched to a depth of 1 mm and a root radius 5 μm using a custom-made razor micro-notcher under irrigation with a 0.05 μm diamond suspension.

To induce collagen network denaturation without damaging the mineral phase of bone, processed samples were divided into heat treatment groups<sup>99</sup>. Collagen is a triple helix, which, when subjected to heat, denatures through unfolding. Non-mineralized collagen in soft tissues denatures through unfolding ~60 °C, and mineralized collagen in bone denatures between 100 °C and 190 °C but mostly around 150 °C<sup>72,74,76,77</sup>. Heat treatments below 200 °C do not alter the composition and the crystal structure of the mineral phase<sup>78–80</sup>. Heat treatment was applied to each sample using an oven for 2 hours in five groups (Room Temperature, 100 °C, 130 °C, 160 °C, 190 °C) to induce different levels of collagen denaturation. Following preparation, samples were submerged in Hank's Balanced Salt Solution (HBSS) for at least 12 hours prior to mechanical testing. The rehydration step reverses bound water loss during heat treatment<sup>85,100</sup>, and serves as an important step for preserving mechanical properties.

**Trypsin-hydroxyproline assay.** The trypsin-hydroxyproline assay was used to determine the amount of collagen damage that resulted from heat treatment. Bone samples ( $N = 8–11$ /group) were demineralized in 10% ethylenediaminetetraacetic acid at pH 8 for 1 week as recommended by Kiviranta et al.<sup>101</sup>. The samples were digested by 500 μL trypsin (T0303 Sigma-Aldrich) for 24 hours. The supernatant containing the denatured collagen was transferred to new vials, and the remaining collagen was left in their original vials and filled with 500 μL of buffer solution. The remaining peptides in the solution were acid-hydrolyzed by 12N HCl and heated at 110 °C for 18 hours. Then, as reported by Brown, chloramine-T solution and p-DAB reagent were added to react with the hydroxyproline residues to provide a colorimetric reading<sup>64</sup>. Finally, hydroxyproline content was obtained using a microplate reader. Absorbance was read at 561 nm and converted to micrograms using a standard hydroxyproline kit (MAK008 Sigma-Aldrich). The amount of denatured collagen was measured from the supernatant vials, and the original vials contain the remaining collagen. The percent of denatured collagen is calculated by comparing the amount of denatured collagen to the total collagen content. The amount of denatured collagen was measured from the supernatant vials, and the amount of intact collagen was measured from the original vials. Then, the percent of denatured collagen was calculated by dividing the amount of denatured collagen over the total collagen content.

**Flexural strength tests.** To assess macroscale mechanical properties, bovine bone samples ( $N = 6–8$ /group) were tested for failure under a 3-point bending flexural strength test in accordance with ASTM D790<sup>102</sup>. Although standards for assessing the material properties of structural materials exist, there are few comprehensive guides for biological materials; as such, ASTM standards for appropriate materials are often adopted in bone research<sup>103</sup>. Flexural strength tests were performed with a span of 25.4 mm, a displacement rate of 0.05 mm/min, and data were recorded at 20 Hz with a lowpass filter cutoff of 100 Hz in a similar way to Acevedo et al.<sup>46</sup>. All bone samples were tested in the transverse orientation, perpendicular to the direction of osteons. To ensure sample hydration, drops of phosphate-buffered saline were poured on a gauze wrapped around each sample. Each test was performed under displacement control using a Psylotech testing device equipped with a 222 N load cell. A preload of 0.5 N was applied prior to testing. During each test, force and displacement data were recorded. All original force-displacement curves are shown in Supplementary Figure 2. Using these data and sample geometry, a strain-stress curve was plotted in MATLAB<sup>104</sup> using equations 3 and 5 from the ASTM D790. From these curves, ultimate strain, work to fracture, and Young's modulus was calculated.

**In situ SR $\mu$ CT imaging and toughness testing.** Imaging and toughness testing was performed on bovine bone samples ( $N = 2/\text{group}$ ) in a custom three-point bending chamber with a span of 6-mm at the Advanced Light Source beamline 8.3.2. - microtomography at Lawrence Berkeley National Laboratory to track crack propagation in near real-time. Prior to any toughness testing, a reference high- and low-quality scan was taken of each sample with 3937 and 657 projections respectively for training the CNN. An incident x-ray energy of 24 keV was selected with an exposure time of 100 ms. Image voxel size was 1.6  $\mu\text{m}/\text{voxel}$ . A 1-mm Aluminum shield was used to limit the radiation dose in the bone sample. The radiation dose was calculated following a similar procedure to Barth et al.<sup>54</sup> and was found to be 10 kGy for the reference high-quality scan and 1–2 kGy for each low-quality scan, keeping the total radiation dose underneath the detrimental limit of 35 kGy for the majority of crack propagation<sup>55</sup>. This indicates that 1 high-dose scan and 11 low-dose scans can be taken before the maximum recommended radiation dose of 35 kGy is exceeded<sup>54,55</sup>. Radiation dose calculations were performed in accordance with estimations performed by Barth et al.<sup>54</sup>. Their used ultraviolet resonance Raman spectroscopy to show that changes in plastic properties can be associated with collagen degradation. This is also supported by other studies on gamma radiation<sup>105–107</sup>.

The testing chamber allowed for sample immersion in HBSS bath during scanning and mechanical testing to ensure the bone tissue remained in physiological conditions. The three-point bending fracture toughness test was performed in accordance with ASTM E1820<sup>108</sup> with constant displacement while simultaneously monitoring the force-displacement output of the load cell in the testing chamber. Bones were mechanically loaded in the transverse direction, normal to the direction of osteons. During the fracture toughness test, the force-displacement curve was observed to determine when crack growth occurred, shown in Supplementary Figure 3. Crack growth was expected when there was a drop in the force-displacement curve. Following a drop in the curve, the displacement was paused and a low-quality scan of the sample was acquired. Following the acquisition of the low-quality scan, the displacement resumed, and the test continued. This procedure of pausing the displacement and acquiring a low-quality scan was repeated for each suspected increment of crack growth until material failure. Each sample took approximately 2 hours to test, with time in between each sample to swap samples and prepare the next test. During each in situ toughness test, the time between steps of suspected crack propagation was  $\sim 7\text{--}9$  minutes. Reconstruction of SR $\mu$ CT data was performed with the Python open-source package Tomopy<sup>109</sup> and visualization was performed in Dragonfly 2020.2 (Object Research Systems (ORS) Inc, Montreal, Canada) and ImageJ<sup>110</sup>.

**R-curve toughness calculation.** Data from the in situ SR $\mu$ CT imaging and toughness test were used to calculate bones resistance to fracture at the various levels of heat treatment ( $N = 2/\text{group}$ ). The procedure and equations used for these calculations can be found in ASTM E1820<sup>108</sup>. The change in crack length,  $\Delta a$ , was measured using SR $\mu$ CT images for each crack growth step. Nonlinear fracture mechanics analysis was used to determine the J-based crack-resistance curves ( $J$  as a function of  $\Delta a$ ). The applied load and  $\Delta a$  values were used to measure the nonlinear strain-energy release rate with elastic and plastic contributions ( $J = J_{el} + J_{pl}$ ) and to calculate the stress-intensity factor ( $K$ ) for each growth step<sup>108</sup>. From the  $K$ , the  $J$  elastic was calculated. We assumed a mode I (tensile opening) stress intensity,  $K_I$  since mode II (shear) fracture toughness was shown to be  $<25\%$  of mode I fracture toughness<sup>111</sup>. The load-displacement data were used to calculate the area under the force-displacement curve ( $A_{pl}$ ) at each step. Following the ASTM E1820,  $J$  plastic was calculated using  $A_{pl}$ , the sample thickness, and the width of the remaining ligament.  $J$  total was calculated by adding the  $J$  elastic and the  $J$  plastic. The  $J$  total was converted back into the J-integral stress intensity ( $K_I$ ) for nominally mode I fracture.  $K_I$  values were plotted against the  $\Delta a$  values for each group to generate R-curves. The Young's modulus used in these calculations were obtained from preliminary flexural tests on similar samples (as described above). To ensure the validity of the method in plane strain conditions, the sample thickness  $B$  (1 mm in this study) was chosen to meet the condition  $B > 2.5(K/\sigma_y)^2$  which is  $\sim 0.25$  mm (for an average initiation toughness  $K$  of 1  $\text{MPa} \cdot \text{m}^{1/2}$  and yield stress of  $\sigma_y$  of 100 MPa). In addition, the crack extension is only valid when it is greater than the plastic zone size,  $r_y = 1/6(K/\sigma_y)^2$  in plane strain conditions. In this case, the plastic zone size is  $r_y = 0.01$  mm. Calculations were performed in MATLAB<sup>104</sup> and Microsoft Excel.

**Mixed-scale dense CNN.** Image denoising and segmentation were performed using a CNN. Denoising improved the quality of images acquired at low radiation, making them usable in further analysis. Segmentation was used to expedite portions of the analysis. The specific network architecture used was the mixed-scale dense CNN developed by Pelt et al.<sup>65</sup>. This network architecture is unique in its ability to capture multi-scale features through mixed-scale dilated convolutions. Here, we present, for the first time, the application of such networks to denoise and segment SR $\mu$ CT images of a real-world in situ experiment, using a dedicated experimental setup for acquiring the required training data. The network was defined with a depth of 100 layers for both denoising and segmentation tasks. The training was performed on a workstation with an Nvidia GeForce GTX 1080Ti GPU on CUDA 10.1.

To train the network for the denoising task, the paired high- and low-quality SR $\mu$ CT reference images were used as training data. These scans were taken before the in situ experiments were performed on each sample. In preparation for training, the images were cropped to a dimension of  $1024 \times 1024$  pixels using ImageJ<sup>110</sup>. This cropping reduced the image size and narrowed the region of interest to make training more efficient. Approximately 650 image slices were used from each viable reference high- and low-quality scan. Of the ten samples tested, three samples were not used during training due to imaging artifacts present in high-quality data or the inability to reconstruct image data. Therefore, a total of seven image volumes were used during training, validation, and testing. A training, validation, and test split of  $\sim 70\text{--}15\text{--}15$  was performed on the cropped images, yielding 3240 training images, 680 validation images, and a holdout test scan of 662 test images. The training images were converted to 3D slabs containing five image slices. These slabs included two consecutive slices before and two slices after the image was denoised to provide the network additional contextual information. The data were input to the network in batch sizes of one and the order of the images was shuffled after each epoch. The training data were augmented using both horizontal and vertical flipping with a probability of 0.5 to mitigate overfitting. Training occurred over 44 epochs using MSE as the loss function and Adam as the optimizer.

Semantic segmentation capabilities of the MS-D net were used in crack segmentation. A training dataset was obtained through manual segmentation of the crack using Dragonfly 2020.2 (Object Research Systems (ORS) Inc, Montreal, Canada). The final time point of crack growth from each of the seven viable samples was manually segmented for ground truth labels used during training. This segmentation was completed using a combination of thresholding and manual selection. A threshold was used to select the background and exclude the bone. Then, using the snap and paint tools in Dragonfly, the regions of the background we identified as cracks were selected. An intermediate network was trained and used to provide a better starting point for the manual segmentation; however, the predictions of the intermediate network were also manually corrected. All segmentations were performed and reviewed by the same two researchers. The segmentations were overlaid on the original image to ensure good segmentation. Approximately 625 image slices were manually segmented from the viable samples. Denoised images of dimension  $1024 \times 1024$  pixels were used as input to the network. The training, validation, test split of  $\sim 70\text{--}15\text{--}15$  was maintained with 3124 training images, 625 validation images, and a holdout test scan of 632 images. Again, input images were arranged into slabs consisting of five images that were input to the network in batch sizes of one. The images were shuffled during training following each epoch. The training data were augmented through horizontal and vertical flipping with a probability of 0.5. To learn the segmentation task, cross-entropy was used as the loss function. Network performance was further evaluated by calculating the Dice similarity coefficient for the segmentation<sup>67</sup>.

**Crack deflection quantification.** Since crack deflection is the dominant extrinsic toughening mechanism, the amount of crack deflection in each sample was quantified ( $N = 1\text{--}2/\text{group}$ ). Crack deflection was measured for each sample at the final time point when the sample had fractured completely. Quantification of crack deflection was a multi-step process calculated using a custom python code (see code availability section). The process begins with the binary image of the crack segmented by the MS-D network. Each segmented crack surface was converted to a skeletonized representation using the median position value between the top and bottom surfaces of the segmented crack, i.e., the median position through the thickness of the crack. The gradient of the skeletonized crack surface in the direction of crack propagation (mode I) was calculated. The gradient of the crack was calculated to determine the points on the crack where a change in direction occurred in the direction of crack growth. This gradient was then smoothed using a rolling average. Following smoothing, large crack deflections were filtered using minimum magnitude and angle thresholds of 50 microns and 30 degrees, respectively. Two samples with insufficient crack propagation or excessive crack bifurcation were excluded from the calculations (100  $^{\circ}\text{C}$ , 160  $^{\circ}\text{C}$ ). To eliminate small crack deflections, the OPTICS clustering algorithm in sci-kit learn was used to group larger sections of crack deflections<sup>112</sup>. The detailed workflow used for this study is shown in Supplementary Figure 4 and in the crack deflection GitHub repo. After large crack deflection events are found using the magnitude and angle thresholds, the average number of deflections normalized by crack length (Df.Dn) and average crack deflection angle (Df.An) are calculated for each sample. Because the sample size is not sufficient for a comparison between each heat-treatment temperature, no statistics were performed on the individual groups. Instead, comparisons were performed on the UC and DC groupings of temperatures using an independent  $t$  test.

**Digital volume correlation.** The internal strain state of samples was visualized and evaluated using DVC ( $N = 1\text{--}2/\text{group}$ ). DVC was performed using the Python-based package TomoWarp<sup>2113</sup> to compare the unloaded reference volume to the deformed volume at different steps of crack growth. Scans that had been denoised using the CNN were cropped to  $400 \times 300 \times 300$  voxels to focus on the region of bone ahead of the crack tip, and exclude regions containing the crack. The cropped scans were segmented into binary images, separating the features of bone (lacunae, canals, and notch) from the bone matrix. These features were tracked during DVC.

For each sample, a correlation window of 25 voxels in all directions and a node spacing of 10 voxels in all directions were chosen. The search window was chosen to include all possible deformations. Data filtering was carried out using functionality in Tomowarp<sup>2113</sup>. Both the outlier and median filters were applied to the displacement data. The strain was calculated using these processed data according to the Green strain functions included in Tomowarp<sup>2113</sup>. The strains were upsampled with first-order, linear interpolation to match the original image dimensions using SciPy<sup>114</sup>. Upsampled strains were written to 32-bit image files for visualization in Dragonfly 2020.2 (Object Research Systems (ORS) Inc, Montreal, Canada)

**Statistics.** The data were compiled and statistical analyses were performed using R. Appropriate statistical methods were used to determine significance. When comparing two groups an unpaired two-tailed Student's *t* test was used. For multiple comparisons, an analysis of variance with a Tukey post hoc test was used. In both cases, statistical difference was determined with an  $\alpha = 0.05$ . In all bar charts, the data are presented as mean  $\pm$  standard deviation.

### Data availability

Data that support the findings of this study are available from the corresponding author upon reasonable request.

### Code availability

Code for denoising and segmenting the low-dose images using the convolutional neural network is available for download at author D.M. Pelt's GitHub page: <https://github.com/dmpelt/msdnet>. Custom code for quantifying crack deflection from segmented SR $\mu$ CT scans is available for download at the Fracture and Fatigue of Skeletal Tissue's GitHub page: <https://github.com/F2-lab/crack-deflection>.

Received: 30 March 2022; Accepted: 26 September 2022;

Published online: 21 October 2022

### References

- Rho, J.-Y., Kuhn-Spearing, L. & Zioupos, P. Mechanical properties and the hierarchical structure of bone. *Med. Eng. Phys.* **20**, 92–102 (1998).
- Nalla, R., Kinney, J. & Ritchie, R. Effect of orientation on the in vitro fracture toughness of dentin: the role of toughening mechanisms. *Biomaterials* **24**, 3955–3968 (2003).
- Launey, M. E. & Ritchie, R. O. On the fracture toughness of advanced materials. *Adv. Mater.* **21**, 2103–2110 (2009).
- Kong, S. H., Hong, N., Kim, J.-W., Kim, D. Y. & Kim, J. H. Application of the trabecular bone score in clinical practice. *J. Bone Metab.* **28**, 101 (2021).
- Diez-Perez, A. et al. Recommendations for a standard procedure to assess cortical bone at the tissue-level in vivo using impact microindentation. *Bone Rep.* **5**, 181–185 (2016).
- Kanis, J. A. et al. Frax<sup>®</sup> and its applications to clinical practice. *Bone* **44**, 734–743 (2009).
- Burr, D. B., Robling, A. G. & Turner, C. H. Effects of biomechanical stress on bones in animals. *Bone* **30**, 781–786 (2002).
- Currey, J. D. The effect of porosity and mineral content on the young's modulus of elasticity of compact bone. *J. Biomech.* **21**, 131–139 (1988).
- Boskey, A., Wright, T. & Blank, R. Collagen and bone strength. *J. Bone Miner. Res.* **14**, 330–335 (1999).
- Wang, X. et al. Effect of collagen denaturation on the toughness of bone. *Clin. Orthop. Relat. Res.* **371**, 228–239 (2000).
- Zioupos, P., Currey, J. & Hamer, A. The role of collagen in the declining mechanical properties of aging human cortical bone. *J. Biomed. Mater. Res.* **45**, 108–116 (1999).
- Li, Y. & Yu, S. M. In situ detection of degraded and denatured collagen via triple helical hybridization: new tool in histopathology. *Methods Mol. Biol.* **1944**, 135–144 (2019).
- Lin, A. H., Zitnay, J. L., Li, Y., Yu, S. M. & Weiss, J. A. Microplate assay for denatured collagen using collagen hybridizing peptides. *J. Orthop. Res.* **37**, 431–438 (2019).
- Wang, X., Shen, X., Li, X. & Agrawal, C. M. Age-related changes in the collagen network and toughness of bone. *Bone* **31**, 1–7 (2002).
- Mirigian, L. S. et al. Collagen degradation by tumor-associated trypsin. *Arch. Biochem. Biophys.* **535**, 111–114 (2013).
- Kuznetsova, N. V., McBride Jr, D. J. & Leikin, S. Changes in thermal stability and microunfolding pattern of collagen helix resulting from the loss of  $\alpha 2$  (i) chain in osteogenesis imperfecta murine. *J. Mol. Biol.* **331**, 191–200 (2003).
- Makareeva, E. et al. Structural heterogeneity of type i collagen triple helix and its role in osteogenesis imperfecta. *J. Biol. Chem.* **283**, 4787–4798 (2008).
- Pereira, R. F., Hume, E. L., Halford, K. W. & Prockop, D. J. Bone fragility in transgenic mice expressing a mutated gene for type i procollagen (col1a1) parallels the age-dependent phenotype of human osteogenesis imperfecta. *J. Bone Miner. Res.* **10**, 1837–1843 (1995).
- Jepsen, K. J. et al. Type i collagen mutation alters the strength and fatigue behavior of mov13 cortical tissue. *J. Biomech.* **30**, 1141–1147 (1997).
- Carriero, A., Zimmermann, E. A., Shefelbine, S. J. & Ritchie, R. O. A methodology for the investigation of toughness and crack propagation in mouse bone. *J. Mech. Behav. Biomed. Mater.* **39**, 38–47 (2014).
- Hollander, A. P. et al. Increased damage to type ii collagen in osteoarthritic articular cartilage detected by a new immunoassay. *J. Clin. Investig.* **93**, 1722–1732 (1994).
- Mann, V. et al. A col1a1 sp1 binding site polymorphism predisposes to osteoporotic fracture by affecting bone density and quality. *J. Clin. Investig.* **107**, 899–907 (2001).
- Bernad, M. et al. Polymorphism in the type i collagen (col1a1) gene and risk of fractures in postmenopausal women. *Bone* **30**, 223–228 (2002).
- Uitterlinden, A. G. et al. Relation of alleles of the collagen type i $\alpha$ 1 gene to bone density and the risk of osteoporotic fractures in postmenopausal women. *N. Engl. J. Med.* **338**, 1016–1021 (1998).
- Bondarenko, L. B. Diabetes and collagen: interrelations. *Avicenna J. Med. Biochem.* **7**, 64–71 (2019).
- Mieczkowska, A. et al. Alteration of the bone tissue material properties in type 1 diabetes mellitus: a fourier transform infrared microspectroscopy study. *Bone* **76**, 31–39 (2015).
- Lin, A. H. et al. Collagen denaturation is initiated upon tissue yield in both positional and energy-storing tendons. *Acta Biomater.* **118**, 153–160 (2020).
- Wright, N. & Humphrey, J. Denaturation of collagen via heating: an irreversible rate process. *Annu. Rev. Biomed. Eng.* **4**, 109–128 (2002).
- Brandts, J. F. Conformational transitions of proteins in water and in aqueous mixtures. In: *Structure and stability of biological macromolecules*. Vol. 2, 213 (1969).
- Privalov, P. Stability of proteins: proteins which do not present a single cooperative system. *Adv. Protein Chem.* **35**, 1–104 (1982).
- Nalla, R. K., Krusic, J. J. & Ritchie, R. O. On the origin of the toughness of mineralized tissue: microcracking or crack bridging? *Bone* **34**, 790–798 (2004).
- Launey, M. E., Buehler, M. J. & Ritchie, R. O. On the mechanistic origins of toughness in bone. *Annu. Rev. Mater. Res.* **40**, 25–53 (2010).
- Depalle, B., Qin, Z., Shefelbine, S. J. & Buehler, M. J. Influence of cross-link structure, density and mechanical properties in the mesoscale deformation mechanisms of collagen fibrils. *J. Mech. Behav. Biomed. Mater.* **52**, 1–13 (2015).
- Oxlund, H., Barckman, M., Ørtoft, G. & Andreassen, T. Reduced concentrations of collagen cross-links are associated with reduced strength of bone. *Bone* **17**, S365–S371 (1995).
- Saito, M. & Marumo, K. Effects of collagen crosslinking on bone material properties in health and disease. *Calcif. Tissue Int.* **97**, 242–261 (2015).
- Fantner, G. E. et al. Sacrificial bonds and hidden length dissipate energy as mineralized fibrils separate during bone fracture. *Nat. Mater.* **4**, 612–616 (2005).
- Nalla, R., Stölken, J., Kinney, J. & Ritchie, R. Fracture in human cortical bone: local fracture criteria and toughening mechanisms. *J. Biomech.* **38**, 1517–1525 (2005).
- Koester, K. J., Ager, J. & Ritchie, R. The true toughness of human cortical bone measured with realistically short cracks. *Nat. Mater.* **7**, 672–677 (2008).
- Ritchie, R. O. How does human bone resist fracture? *Ann. N. Y. Acad. Sci.* **1192**, 72–80 (2010).
- Nalla, R. K., Kinney, J. H. & Ritchie, R. O. Mechanistic fracture criteria for the failure of human cortical bone. *Nat. Mater.* **2**, 164–168 (2003).
- Nalla, R. et al. Role of microstructure in the aging-related deterioration of the toughness of human cortical bone. *Mater. Sci. Eng.* **26**, 1251–1260 (2006).
- Chan, K. S., Chan, C. K. & Nicoletta, D. P. Relating crack-tip deformation to mineralization and fracture resistance in human femur cortical bone. *Bone* **45**, 427–434 (2009).
- Zimmermann, E. A., Launey, M. E. & Ritchie, R. O. The significance of crack-resistance curves to the mixed-mode fracture toughness of human cortical bone. *Biomaterials* **31**, 5297–5305 (2010).
- Salomé, M. et al. A synchrotron radiation microtomography system for the analysis of trabecular bone samples. *Med. Phys.* **26**, 2194–2204 (1999).
- Spanne, P. & Rivers, M. L. Computerized microtomography using synchrotron radiation from the NSLS. *Nucl. Instrum. Methods Phys. Res. B* **24**, 1063–1067 (1987).
- Acevedo, C. et al. Alendronate treatment alters bone tissues at multiple structural levels in healthy canine cortical bone. *Bone* **81**, 352–363 (2015).
- Zimmermann, E. A., Busse, B. & Ritchie, R. O. The fracture mechanics of human bone: influence of disease and treatment. *Bonekey Rep.* **4**, 743 (2015).

48. Peterlik, H., Roschger, P., Klaushofer, K. & Fratzl, P. From brittle to ductile fracture of bone. *Nat. Mater.* **5**, 52–55 (2006).
49. Yan, L. et al. A method for fracture toughness measurement in trabecular bone using computed tomography, image correlation and finite element methods. *J. Mech. Behav. Biomed. Mater.* **109**, 103838 (2020).
50. Liu, L. & Morgan, E. F. Accuracy and precision of digital volume correlation in quantifying displacements and strains in trabecular bone. *J. Biomech.* **40**, 3516–3520 (2007).
51. Le Cann, S. et al. Investigating the mechanical characteristics of bone-metal implant interface using in situ synchrotron tomographic imaging. *Front. Bioeng. Biotechnol.* **6**, 208 (2019).
52. Le Cann, S., Tudisco, E., Tägil, M., Hall, S. A. & Isaksson, H. Bone damage evolution around integrated metal screws using x-ray tomography-in situ pullout and digital volume correlation. *Front. Bioeng. Biotechnol.* **8**, 934 (2020).
53. Turunen, M. J. et al. Sub-trabecular strain evolution in human trabecular bone. *Sci. Rep.* **10**, 1–14 (2020).
54. Barth, H. D., Launey, M. E., MacDowell, A. A., Ager III, J. W. & Ritchie, R. O. On the effect of x-ray irradiation on the deformation and fracture behavior of human cortical bone. *Bone* **46**, 1475–1485 (2010).
55. Barth, H. D. et al. Characterization of the effects of x-ray irradiation on the hierarchical structure and mechanical properties of human cortical bone. *Biomaterials* **32**, 8892–8904 (2011).
56. Fernández, M. P. et al. Effect of sr-microct radiation on the mechanical integrity of trabecular bone using in situ mechanical testing and digital volume correlation. *J. Mech. Behav. Biomed. Mater.* **88**, 109–119 (2018).
57. Yang, X. et al. Low-dose x-ray tomography through a deep convolutional neural network. *Sci. Rep.* **8**, 1–13 (2018).
58. Hendriksen, A. A. et al. Deep denoising for multi-dimensional synchrotron x-ray tomography without high-quality reference data. *Sci. Rep.* **11**, 1–13 (2021).
59. Liu, Z. et al. Tomogan: low-dose synchrotron x-ray tomography with generative adversarial networks: discussion. *JOSA A* **37**, 422–434 (2020).
60. Anwar, S. M. et al. Medical image analysis using convolutional neural networks: a review. *J. Med. Syst.* **42**, 1–13 (2018).
61. Kadler, K. E., Hojima, Y. & Prockop, D. Assembly of type I collagen fibrils de novo between 37 and 41 degrees c the process is limited by micro-unfolding of monomers. *J. Biol. Chem.* **263**, 10517–10523 (1988).
62. Ryhänen, L., Zaragoza, E. J. & Uitto, J. Conformational stability of type I collagen triple helix: evidence for temporary and local relaxation of the protein conformation using a proteolytic probe. *Arch. Biochem. Biophys.* **223**, 562–571 (1983).
63. Westerhausen, A., Kishi, J. & Prockop, D. J. Mutations that substitute serine for glycine alpha 1-598 and glycine alpha 1-631 in type I procollagen. the effects on thermal unfolding of the triple helix are position-specific and demonstrate that the protein unfolds through a series of cooperative blocks. *J. Biol. Chem.* **265**, 13995–14000 (1990).
64. Brown, S., Worsfold, M. & Sharp, C. Microplate assay for the measurement of hydroxyproline in acid-hydrolyzed tissue samples. *Biotechniques* **30**, 38–42 (2001).
65. Pelt, D. M. & Sethian, J. A. A mixed-scale dense convolutional neural network for image analysis. *Proc. Natl. Acad. Sci. USA* **115**, 254–259 (2018).
66. Lehtinen, J. et al. Noise2noise: learning image restoration without clean data. arXiv preprint arXiv:1803.04189 (2018).
67. Zou, K. H. et al. Statistical validation of image segmentation quality based on a spatial overlap index: scientific reports. *Academi. Radiol.* **11**, 178–189 (2004).
68. Schuit, S. et al. Fracture incidence and association with bone mineral density in elderly men and women: the rotterdam study. *Bone* **34**, 195–202 (2004).
69. Wainwright, S. A. et al. Hip fracture in women without osteoporosis. *J. Clin. Endocrinol. Metab.* **90**, 2787–2793 (2005).
70. Felsenberg, D. & Boonen, S. The bone quality framework: determinants of bone strength and their interrelationships, and implications for osteoporosis management. *Clin. Ther.* **27**, 1–11 (2005).
71. Dempster, D., Felsenberg, D. & van der Geest, S. The bone quality book, a guide to factors influencing bone strength. In: *Excerpta Medica* (2006).
72. Todoh, M., Tadano, S. & Imari, Y. Effect of heat denaturation of collagen matrix on bone strength. In: *13th international conference on biomedical engineering*, 2034–2037 (Springer, 2009).
73. Yamashita, J. et al. Collagen and bone viscoelasticity: a dynamic mechanical analysis. *J. Biomed. Mater. Res.* **63**, 31–36 (2002).
74. Kronick, P. L. & Cooke, P. Thermal stabilization of collagen fibers by calcification. *Connect. Tissue Res.* **33**, 275–282 (1996).
75. Trkebacz, H. & Wójtowicz, K. Thermal stabilization of collagen molecules in bone tissue. *Int. J. Biol. Macromol.* **37**, 257–262 (2005).
76. Bonar, L. C. & Glimcher, M. J. Thermal denaturation of mineralized and demineralized bone collagens. *J. Ultrastruct. Res.* **32**, 545–557 (1970).
77. Danielsen, C. C. Thermal stability of human-fibroblast-collagenase-cleavage products of type-I and type-III collagens. *Biochem. J.* **247**, 725–729 (1987).
78. Wang, X., Bank, R. A., TeKoppele, J. M. & Agrawal, C. M. The role of collagen in determining bone mechanical properties. *J. Orthop. Res.* **19**, 1021–1026 (2001).
79. Holden, J., Clement, J. & Phakey, P. Age and temperature related changes to the ultrastructure and composition of human bone mineral. *J. Bone Miner. Res.* **10**, 1400–1409 (1995).
80. Holden, J., Phakey, P. & Clement, J. Scanning electron microscope observations of heat-treated human bone. *Forensic Sci. Int.* **74**, 29–45 (1995).
81. Catanese III, J., Featherstone, J. & Keaveny, T. M. Characterization of the mechanical and ultrastructural properties of heat-treated cortical bone for use as a bone substitute. *J. Biomed. Mater. Res.* **45**, 327–336 (1999).
82. Fantner, G. E. et al. Influence of the degradation of the organic matrix on the microscopic fracture behavior of trabecular bone. *Bone* **35**, 1013–1022 (2004).
83. Yan, J., Daga, A., Kumar, R. & Mecholsky, J. J. Fracture toughness and work of fracture of hydrated, dehydrated, and ashed bovine bone. *J. Biomech.* **41**, 1929–1936 (2008).
84. Granke, M., Does, M. D. & Nyman, J. S. The role of water compartments in the material properties of cortical bone. *Calcif. Tissue Int.* **97**, 292–307 (2015).
85. Luckasansombool, P., Higgs, W., Higgs, R. & Swain, M. Fracture toughness of bovine bone: influence of orientation and storage media. *Biomaterials* **22**, 3127–3132 (2001).
86. Pezzotti, G. & Sakakura, S. Study of the toughening mechanisms in bone and biomimetic hydroxyapatite materials using raman microprobe spectroscopy. *J. Biomed. Mater. Res. A* **65**, 229–236 (2003).
87. Bonfield, W., Grynypas, M. & Young, R. Crack velocity and the fracture of bone. *J. Biomech.* **11**, 473–479 (1978).
88. Wright, T. & Hayes, W. Fracture mechanics parameters for compact bone-effects of density and specimen thickness. *J. Biomech.* **10**, 419–430 (1977).
89. Ebacher, V. & Wang, R. A unique microcracking process associated with the inelastic deformation of haversian bone. *Adv. Funct. Mater.* **19**, 57–66 (2009).
90. Koester, K., Barth, H. & Ritchie, R. Effect of aging on the transverse toughness of human cortical bone: evaluation by r-curves. *J. Mech. Behav. Biomed. Mater.* **4**, 1504–1513 (2011).
91. Willett, T. L., Dapaah, D. Y., Uppuganti, S., Granke, M. & Nyman, J. S. Bone collagen network integrity and transverse fracture toughness of human cortical bone. *Bone* **120**, 187–193 (2019).
92. Zioupos, P., Kirchner, H. O. & Peterlik, H. Ageing bone fractures: the case of a ductile to brittle transition that shifts with age. *Bone* **131**, 115176 (2020).
93. Christen, D. et al. Deformable image registration and 3d strain mapping for the quantitative assessment of cortical bone microdamage. *J. Mech. Behav. Biomed. Mater.* **8**, 184–193 (2012).
94. Peña Fernández, M. et al. Preservation of bone tissue integrity with temperature control for in situ sr-microct experiments. *Materials* **11**, 2155 (2018).
95. Fernández, M. P. et al. Time-resolved in situ synchrotron-microct: 4d deformation of bone and bone analogues using digital volume correlation. *Acta Biomater.* **131**, 424–439 (2021).
96. Lipson, S. F. & Katz, J. L. The relationship between elastic properties and microstructure of bovine cortical bone. *J. Biomech.* **17**, 231–240 (1984).
97. Abdel-Wahab, A. A., Alam, K. & Silberschmidt, V. V. Analysis of anisotropic viscoelastoplastic properties of cortical bone tissues. *J. Mech. Behav. Biomed. Mater.* **4**, 807–820 (2011).
98. Manilay, Z., Novitskaya, E., Sadovnikov, E. & McKittrick, J. A comparative study of young and mature bovine cortical bone. *Acta Biomater.* **9**, 5280–5288 (2013).
99. Snow, T. et al. Effect of collagen damage induced by heat treatment on the mixed-mode fracture behavior of bovine cortical bone under elevated loading rates. *Int. J. Fracture* **233**, 85–101 (2022).
100. Nalla, R. K., Kinney, J. H., Tomsia, A. P. & Ritchie, R. O. Role of alcohol in the fracture resistance of teeth. *J. Dent. Res.* **85**, 1022–1026 (2006).
101. Kiviranta, I., Tammi, M., Lappalainen, R., Kuusela, T. & Helminen, H. The rate of calcium extraction during edta decalcification from thin bone slices as assessed with atomic absorption spectrophotometry. *Histochemistry* **68**, 119–127 (1980).
102. ASTM, I. Standard test methods for flexural properties of unreinforced and reinforced plastics and electrical insulating materials. ASTM D790-10 (2010).
103. Ritchie, R. et al. Measurement of the toughness of bone: a tutorial with special reference to small animal studies. *Bone* **43**, 798–812 (2008).
104. MATLAB. 9.7.0.1190202 (R2019b) (The MathWorks Inc., Natick, Massachusetts, 2018).
105. Colwell, A., Hamer, A., Blumsohn, A. & Eastell, R. To determine the effects of ultraviolet light, natural light and ionizing radiation on pyridinium cross-links in bone and urine using high-performance liquid chromatography. *Eur. J. Clin. Invest.* **26**, 1107–1114 (1996).
106. Nguyen, H., Morgan, D. A. & Forwood, M. R. Sterilization of allograft bone: effects of gamma irradiation on allograft biology and biomechanics. *Cell Tissue Bank* **8**, 93–105 (2007).

107. Akkus, O., Belaney, R. M. & Das, P. Free radical scavenging alleviates the biomechanical impairment of gamma radiation sterilized bone tissue. *J. Orthop. Res.* **23**, 838–845 (2005).
108. Standard Test Method for Measurement of Fracture Toughness. Standard, ASTM International, (West Conshohocken, PA 2020).
109. Gürsoy, D., De Carlo, F., Xiao, X. & Jacobsen, C. Tomopy: a framework for the analysis of synchrotron tomographic data. *J. Synchrotron Radiat.* **21**, 1188–1193 (2014).
110. Schindelin, J. et al. Fiji: an open-source platform for biological-image analysis. *Nat. Methods* **9**, 676–682 (2012).
111. Zimmermann, E. A., Launey, M. E., Barth, H. D. & Ritchie, R. O. Mixed-mode fracture of human cortical bone. *Biomaterials* **30**, 5877–5884 (2009).
112. Pedregosa, F. et al. Scikit-learn: machine learning in python. *J. Mach. Learn. Res.* **12**, 2825–2830 (2011).
113. Tudisco, E., Andò, E., Cailletaud, R. & Hall, S. A. Tomowarp2: a local digital volume correlation code. *SoftwareX* **6**, 267–270 (2017).
114. Virtanen, P. et al. SciPy 1.0: fundamental algorithms for scientific computing in python. *Nat. Methods* **17**, 261–272 (2020).
115. Zimmermann, E. A. et al. Age-related changes in the plasticity and toughness of human cortical bone at multiple length scales. *Proc. Natl. Acad. Sci. USA* **108**, 14416–14421 (2011).

### Acknowledgements

This work received support from the National Science Foundation under NSF CAREER Grant CMMI 2045363, and from the University of Utah seed grant (VPR Research Incentive 51900367 for Y.O.). This work was supported in part by NIOSH #5T42OH008414-16. The opinions and findings of the authors do not necessarily reflect the view and opinions of NIOSH. This work also used resources from the Advanced Light Source at beamline 8.3.2., a U.S. DOE Office of Science User Facility under contract no. DE-AC02-05CH11231. D.M. Pelt is supported by The Netherlands Organization for Scientific Research (NWO), project number 016.Veni.192.235.

### Author contributions

C.A. designed research; M.S. and Y.O. performed research; M.S., Y.O., J.L.R. and W.W. analyzed data; D.M.P. constructed neural network; D.Y.P. and H.S.B. assisted in beamline

operation; M.S., Y.O., and C.A. wrote the manuscript. All authors have given approval for the final version of the manuscript.

### Competing interests

The authors declare no competing interests.

### Additional information

**Supplementary information** The online version contains supplementary material available at <https://doi.org/10.1038/s43246-022-00296-6>.

**Correspondence** and requests for materials should be addressed to Claire Acevedo.

**Peer review information** *Communications Materials* thanks the anonymous reviewers for their contribution to the peer review of this work. Primary Handling Editor: John Plummer.

**Reprints and permission information** is available at <http://www.nature.com/reprints>

**Publisher's note** Springer Nature remains neutral with regard to jurisdictional claims in published maps and institutional affiliations.



**Open Access** This article is licensed under a Creative Commons Attribution 4.0 International License, which permits use, sharing, adaptation, distribution and reproduction in any medium or format, as long as you give appropriate credit to the original author(s) and the source, provide a link to the Creative Commons license, and indicate if changes were made. The images or other third party material in this article are included in the article's Creative Commons license, unless indicated otherwise in a credit line to the material. If material is not included in the article's Creative Commons license and your intended use is not permitted by statutory regulation or exceeds the permitted use, you will need to obtain permission directly from the copyright holder. To view a copy of this license, visit <http://creativecommons.org/licenses/by/4.0/>.

© The Author(s) 2022